metals

MDPI

Communication

Revealing the Formation of Recast Layer around the Film Cooling Hole in Superalloys Fabricated Using Electrical Discharge Machining

Zenan Yang [1], Lu Liu [2], Jianbin Wang [2], Junjie Xu [1], Wanrong Zhao [1], Liyuan Zhou [1], Feng He [2] and Zhijun Wang [2,*]

[1] Science and Technology on Advanced High-Temperature Structural Materials Laboratory, Beijing Institute of Aeronautical Materials, Beijing 100095, China
[2] State Key Laboratory of Solidification Processing, Northwestern Polytechnical University, Xi'an 710072, China
* Correspondence: zhjwang@nwpu.edu.cn; Tel.: +86-134-8467-1484

Abstract: A film cooling hole is an efficient and reliable cooling method, which is widely used in aeroengine turbine blades to effectively improve the thrust–weight ratio of the engine. Electrical discharge machining is the most common manufacturing process for film cooling holes. Due to the rapid quenching after high-temperature melting, a certain thickness of the recast layer will be formed in the vicinity of the hole wall. The microstructure of the recast layer is considered to be an important factor affecting the performance of single-crystal blades. Generally, the recast layer has been thought of as one of the main reasons for the failure of turbine blades. Accordingly, the formation of the recast layer is an important and interesting issue to be revealed. In this work, the recast layer formed using electrical discharge machining on a single-crystal superalloy is studied with TEM. It is found that the recast layer is in the state of supersaturated solution with a single-crystal structure epitaxially grown from the matrix, and many dislocations were observed therein.

Keywords: film cooling hole; electrical discharge machining; recast layer; microstructure

check for updates

Citation: Yang, Z.; Liu, L.; Wang, J.; Xu, J.; Zhao, W.; Zhou, L.; He, F.; Wang, Z. Revealing the Formation of Recast Layer around the Film Cooling Hole in Superalloys Fabricated Using Electrical Discharge Machining. *Metals* **2023**, *13*, 695. https://doi.org/10.3390/met13040695

Academic Editor: Andrey Belyakov

Received: 20 February 2023
Revised: 25 March 2023
Accepted: 31 March 2023
Published: 3 April 2023

Copyright: © 2023 by the authors. Licensee MDPI, Basel, Switzerland. This article is an open access article distributed under the terms and conditions of the Creative Commons Attribution (CC BY) license (https://creativecommons.org/licenses/by/4.0/).

1. Introduction

Along with the increasing demand for turbine inlet temperature of aeroengines, the thermal barrier coatings and film cooling holes on single-crystal, nickel-based superalloys blades have become an effective way to improve cooling efficiency [1–3]. Film cooling technology is an important innovation that was first applied to the anti-icing of aircraft wings [4]. The discrete holes on the blade's surface with cooling gas passing through can isolate the blade's surface from high temperatures, playing a dual role in heat insulation and cooling. The film cooling holes distributed in turbine blades of aeroengines have several typical characteristics [5]. The aperture of the film cooling hole is very small, approximately in the region of 0.25~1.25 mm. Film cooling holes at different positions may have different crystalline directions. There are also a large number of film holes in a single turbine blade, which may be more than thousands. The distribution characteristics of film cooling holes in the blade make it difficult for the traditional forming processes to meet the requirements. The formation of the recast layer (RL) in the electrical discharge machining (EDM) process has been paid attention to for a long time since it has been thought of as one of the main reasons for the fracture of film cooling holes.

The processing of film cooling holes mainly relies on special processing methods such as EDM, laser drilling (LD) and electro-chemical machining (ECM). Up to now, EDM was the preferred method for manufacturing film cooling holes [6]. The EDM drilling process is mainly composed of a rotating hollow tubular electrode, a high-voltage working fluid and a machined workpiece [7]. The processing principle is to use the pulse discharge between the electrodes to etch the workpiece material while introducing a high-voltage working fluid into the tubular electrode to flush away the machining debris and ensure

the normal discharge of the next pulse [8]. Due to the thermal etching process in EDM, most of the melted and vaporized metals during the thermal etching stage are thrown into the coolant and become small particles, while the remaining part is rapidly cooled and resolidified on the wall and blades surface to form the RL. There is also an adjacent heat-affected zone (HAZ) below the RL [9]. The formation of the RL in the EDM process has been paid attention to for a long time [10,11] since it has been thought of as one of the main reasons for the fracture of film cooling holes.

Previous investigations focused on the factors affecting the recast layer, including processing parameters and the different types of materials. Using the thermal–thermal coupling model, Tang et al. [12,13] reported that most molten metal would remain in the spark pits during a single discharge process to form the recast layer. The material in the process greatly affects the structure of the recast layer. Cusanelli et al. [14] found that due to the presence of carbon, the RL mainly consisted of residual austenite and columnar martensite, and the hardness of the RL was twice that of the ferritic matrix for EDM on W300 steel. Murray et al. [15] found that the RL in monocrystalline silicon was composed of two crystal grains with an amorphous phase. Liu et al. [16] investigated the composition and microstructure of the RL on a nickel–titanium memory alloy and identified that the RL produced using EDM alloy was crystalline.

For the recast layer around the cooling hole of the single-crystal superalloy, the IN738 superalloy, as one of the representative nickel-based precipitation hardening alloys, tends to form a single-crystal structure, and the composition distribution is uniform [17]. Dong et al. [18] investigated two single-crystal superalloys, IC21 and N5, for EDM and found that the composition of the RL can be considered as an imperfect single-crystal structure. On this basis, Shang et al. [19] further confirmed that the RL does not contain a precipitated strengthening phase, and the microhardness is smaller than that of the matrix. The rapid melting and solidification process will lead to defect formation in single-crystal superalloys. In the present work, the superalloys used in turbine blades have gradually developed into the fourth generation with increasing volume fraction of precipitation. A deeper observation at the nanoscale is still limited, and the formation of the RL in alloys with high-volume fraction precipitation also needs to be revealed. This work introduces high-resolution transmission electron microscopy to clarify the nanostructure of the recast layer.

2. Experimental Methods

The single-crystal superalloy used in this study is a fourth-generation superalloy with an approximately 70% volume fraction of precipitation. The chemical composition of the alloy is shown in Table 1.

Table 1. Nominal chemical composition of the fourth-generation, nickel-based, single-crystal superalloy (mass fraction/%) [20].

Element	Cr	Co	Mo	W	Ta	Re	Ru	Nb	Al	Hf	C	Ni
mass fraction/%	2.0~4.0	7.0~10.0	0.8~1.6	6.0~8.0	7.0~9.0	3.0~5.0	2.0~4.0	0.2~1.0	5.0~6.0	0.1~0.3	0.008	Bal.

The film cooling holes were machined on the single-crystal superalloy using EDM. The machining diameter of the film cooling hole is Φ = 0.5 mm, the hole depth is 2 mm, and the hole axis is perpendicular to the surface of the sample. Among the adjustable parameters, the regulation range of pulse width in the electrical parameters is 3~11 μs, the pulse interval is between 8 and 16 μs and the peak current is regulated between 2 and 11 A. The electrode speed and flushing pressure in the non-electric parameters are regulated between 50 and 250 rpm and 0.2 and 0.6 MPa, respectively. The influence of process parameters on the processing quality and efficiency of film cooling holes is different. When the pulse width is 4 μs, the pulse interval is 16 μs, the peak current is 4 A, the electrode rotation speed is 150 rpm and the flushing pressure is 0.4 MPa, the film cooling

hole with better processing quality can be obtained, and, especially, the thickness of the recast layer is thinner and uniform.

Due to the small range of the recast layer, the transmission electron microscopy (TEM) samples were prepared using a focused ion beam (FIB) in SEM (FEI Helios G4 CX). Firstly, the film cooling hole with a thick recast layer was selected with SEM, and then the sample was cut around the hole where the recast layer thickness was uniform. The nanostructure is observed with high-resolution TEM (HR-TEM) of JEM-ARM300F. Figure 1 shows the procedures of the initial lift-out and final thinning. Selecting the specified region is shown in Figure 1a,b. A Ga ion beam is used to mill away trenches adjacent to the region, as shown in Figure 1c. The sample then was handled and welded to a prefabricated Cu-grid and thinned from each side to the desired thickness, as shown in Figure 1d. The range of the recast layer and matrix in the sample is shown in Figure 1d. The clear boundary between the RL and the matrix can be seen in Figure 1.

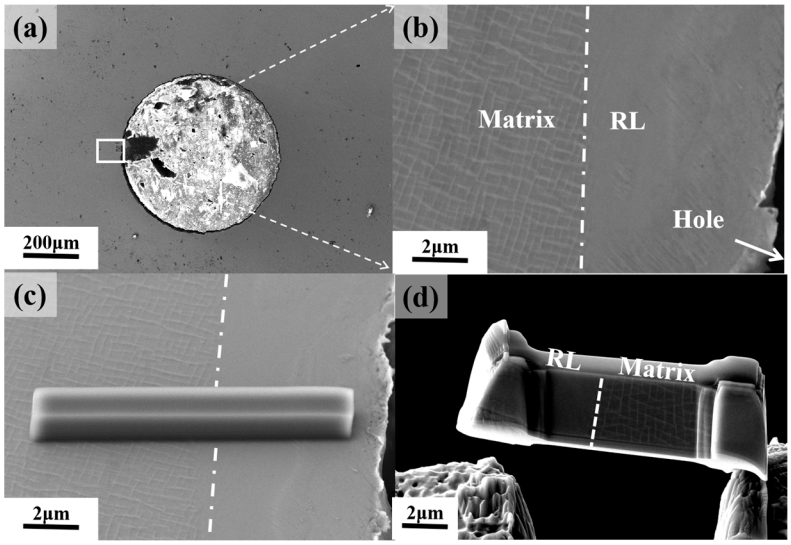


Figure 1. TEM sample preparation: (**a**) The selected specified region with both the matrix and recast layer. (**b**) Microstructure of the selected region. (**c**) The exact location of the TEM sample. (**d**) The prepared sample using FIB. The recast layer (left) and matrix (right) are shown in the sample.

The hardness difference between the recast layer and matrix was investigated using a Hysitron Ti950 nanoindentation with a Berkovich tip, which was calibrated on a standardized fused quartz specimen. The loading and saturation times were set to 5 s and 2 s, respectively. In the side wall of the film cooling hole along the matrix direction, at every 8 μm, a point was pressured, and in the vertical direction of the hole side wall, at every 5 μm, a point was pressured, for a total of 6 points.

3. Results of the Characterizations of the Recast Layer

Figure 2 shows a scanning transmission electron microscopy high angle annular dark field (STEM-HAADF) image of the sample. There are three different regions, which are marked as RL, RL–matrix, and matrix in Figure 2a, which were selected for further TEM analyses. It is obvious that the recast layer and the matrix show a significantly different microstructure. In the matrix, the typical γ′-cube precipitation is regularly distributed in the γ phase, while in the recast layer, the uniform image indicates a single-phase structure without any precipitation. As illustrated in Figure 2b,c, both the dark field (DF) and bright field (BF) images show a large number of dislocations distributing in the recast layer, while the matrix consists of the γ channel and cubical γ′ phase (Figure 2f,g). A clear boundary can be detected between the RL and the matrix, as shown in Figure 2d,e.

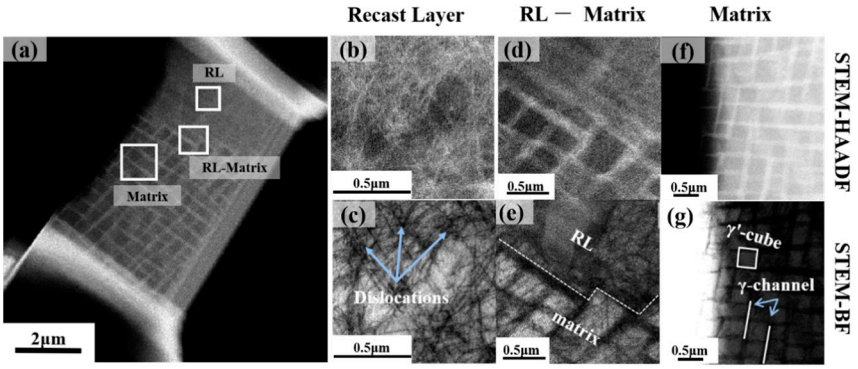


Figure 2. The detailed TEM analysis for the prepared sample: (**a**) The STEM-HAADF image of the overall microstructure. STEM-HAADF and STEM-BF images of (**b**,**c**) the recast layer, (**d**,**e**) the recast layer (RL) and matrix transition area and (**f**,**g**) the matrix of the sample. High-density dislocations are distributed over the area of the recast layer, while the matrix shows a typical γ′-γ microstructure.

To further identify the phase compositions of the two regions, the selected area electron diffraction (SAED) patterns of the recast layer and the matrix are presented in Figure 3. The diffraction patterns in the recast layer and the matrix were obtained under the same tilting condition. The BF image and corresponding SAED pattern in Figure 3a,b indicate that the RL consists of only a single FCC phase. Meanwhile, the SAED pattern in the matrix in Figure 3c,d shows the superlattice of the $L1_2$ phase, corresponding to the γ′ precipitation. Combined with Figure 2, it reveals that after high-temperature melting and rapid quenching, the epitaxial growth of molten metal occurs from the single-crystal matrix, and the same crystal orientation is maintained as the same as the matrix. The excessive cooling rate prevents the precipitation of the γ′ phase during the rapid solidification process. The recast layer continuously formed along the matrix with epitaxial growth is related to the continuous molten pool and temperature gradient generated during EDM. Each molten pool formed in the drilling process can be considered distributed perpendicular to the inner surface of the hole. This means that the molten pool is distributed in the same plane around the hole along the axial direction on the cross-section of the recast layer. The directional temperature gradient of the molten pool ensures the single-crystal properties of the matrix and the recast layer after processing.

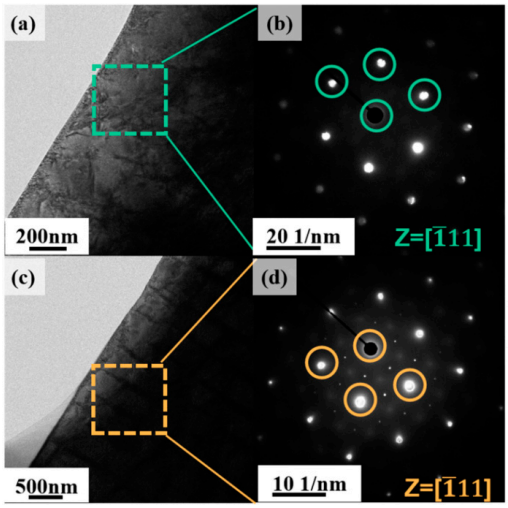


Figure 3. Selected area electron diffraction patterns of (**a**,**b**) the recast layer and (**c**,**d**) the matrix. The recast layer has a single-crystal structure with the same orientation in matrix.

The composition of the recast layer and matrix were also identified with EDS in TEM. As shown in Figure 4, Cr, Co and Re are concentrated in the γ phase of the selected matrix region, while this phenomenon does not exist in the recast layer region. The other

elements do not vary significantly between the two regions. It is also shown that there is no compositional segregation in the recast layer, which further proves that no new phase is generated during the formation of the recast layer, which is consistent with the STEM and SAED analysis. The homogeneous redistribution of the elements in the recast layer is related to the rapid solidification experienced by the alloy in the process of electrical discharge. The alloy melts after reaching the melting point, and the elements are redistributed uniformly in the liquid. Then, the fast cooling leads to the absence of segregation, and there is no solute diffusion in the liquid. Accordingly, the recast layer only forms a single γ phase.

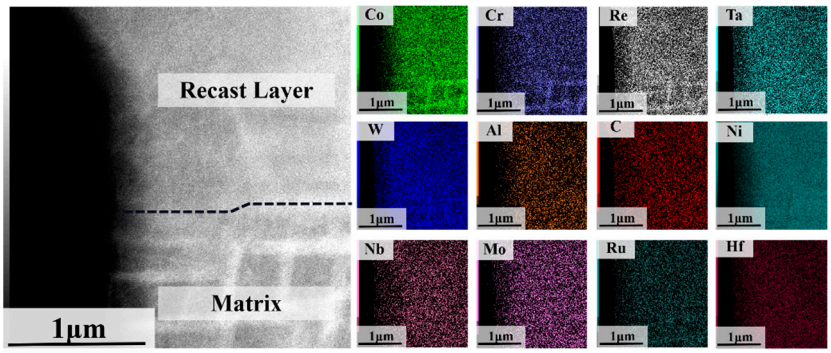


Figure 4. Energy dispersive spectroscopy area scanning profiles of the recast layer and matrix transition region. The composition of the recast layer area is uniform, and there is no segregation for all the elements.

Figure 5 shows the high-resolution TEM (HR-TEM) images and geometric phase analysis of the recast layer and the matrix. The lattice spacing of $(\bar{1}11)$ plane is estimated as 0.2099 nm in the recast layer, which is slightly larger than the lattice spacing of the FCC matrix (Figure 5(a1,a2)). The larger lattice constant of the recast layer is due to the supersaturation of elements with larger atomic sizes. The alloying elements with large atomic radii are dissolved in the recast layer, resulting in a larger lattice constant than that of the matrix. This is consistent with the results shown in Figure 4.

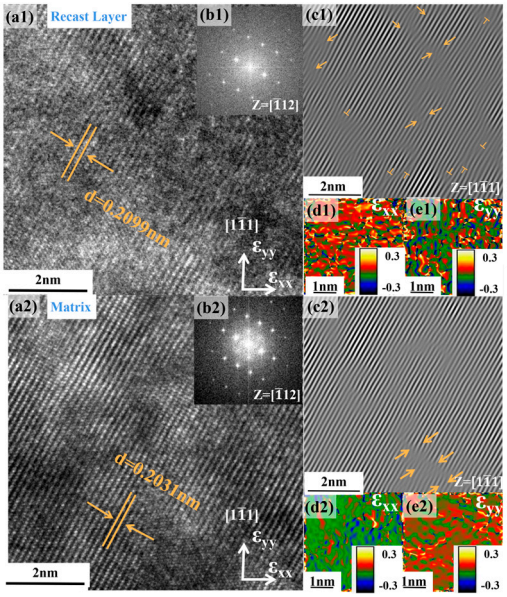


Figure 5. High-resolution transmission electron microscopy analyses of the recast layer (**a1**–**e1**) and the matrix (**a2**–**e2**). (**a1**,**a2**) HR-TEM atomic interface topographies. (**b1**,**b2**) Fast Fourier transform images. (**c1**,**c2**) Inverse fast Fourier transform images. (**d1**,**d2**) Geometric phase analysis (GPA) in the x direction. (**e1**,**e2**) Geometric phase analysis in the y direction. The atomic distortion and dislocation distribution in the recast layer region is more obvious than in the matrix.

Using geometric phase analysis (GPA), it is found that there is a wide range of strain concentration areas in the given x and y directions of the recast layer (Figure 5(d1,e1)), which is due to the high density of dislocations in the recast layer (Figure 5(c1)). Moreover, the microscopic strain of the matrix itself is less obvious (Figure 5(d2,e2)). The differences in lattice constants and microscopic strains between the recast layer and the matrix are closely related to the large number of dislocation defects caused by residual stress during machining, i.e., during the formation of the recast layer, it will be affected by multiple pulse discharges. With the increase in discharge times, the internal residual stress will gradually increase. In the process of forming the recast layer, there will be more dislocation density, resulting in more obvious distortion in the crystal lattice. This is one of the important reasons why there are more strain concentration areas in the recast layer in nanoscale GPA analyses.

According to the analyses shown in Figure 2b,e, under the STEM of the FIB sample, there is a clear boundary between the recast layer and the matrix transition interface, which indicates that the transition area is very small. In order to determine the range of the heat-affected zone more accurately, the diffraction pattern difference and lattice constant change in the recast layer and the matrix on both sides of the interface are explored using a high-resolution transmission image. Figure 6a shows the high-resolution transmission image (view field of 35 nm × 35 nm) near the transition region in the FIB sample. Figure 6b,d shows the corresponding recast layer and matrix regions. Figure 6c,e shows the corresponding diffraction patterns in different regions. It reveals that the distance between the [$\bar{1}$12] atomic plane in the recast layer is larger than that in the matrix. The position of the transition interface can be determined in this way. At the same time, the microstrain inside the heat-affected zone is analyzed. The geometric phase analysis of the microscopic strain distribution in the transition region is further shown in Figure 6f,g. There are differences in the microscopic strain distribution in the transition interface in the x and y directions. The strain in the x direction near the matrix is mainly compressive strain, and the strain in the x direction near the recast layer is mainly tensile strain. This is mainly caused by the difference in the lattice constant of the recast layer and the matrix. The strain on both sides of the *y*-axis direction is tensile strain. The crystal structure in both the recast layer and the matrix is FCC, but the lattice constant of the recast layer is larger than that of the matrix due to the single-phase structure and uniform distribution of elements. The strain in the x-direction difference in the transition region indicates the difference in the atomic arrangement between the recast layer and the matrix and explains the existence of a certain degree of misorientation between the recast layer and the matrix.

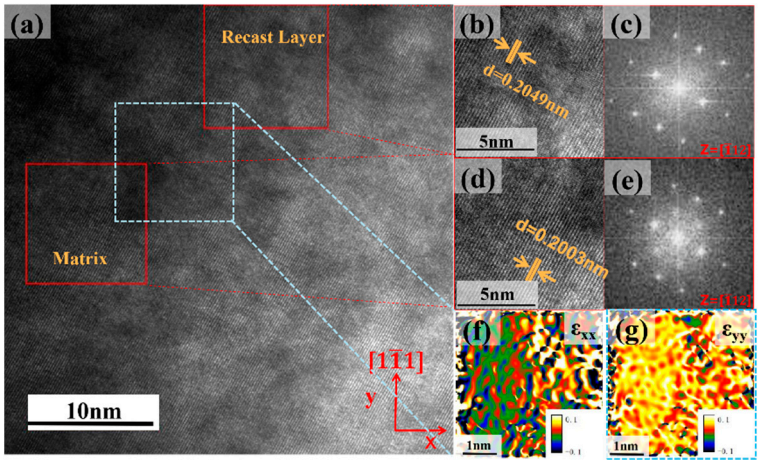


Figure 6. HR-TEM analysis of transition regions: (**a**) HR-TEM image; (**b**,**c**) HR-TEM and FFT of the recast layer; (**d**,**e**) HR-TEM and FFT of the matrix; and (**f**,**g**) geometric phase analysis of transition regions along the x and y directions.

4. Discussion

As the main result of the rapid melting and solidification process, the recast layer has many unique characteristics in terms of the forming method and structure compared with other materials. When the high-power energy of the single-crystal superalloy is given instantaneously, a directional temperature gradient will appear in the molten pool. The recast layer will achieve epitaxial growth along the direction of the single-crystal matrix during the high-temperature melting and rapid solidification process, maintain a continuous crystal orientation and finally grow into a single-crystal structure connected to the matrix material. For the discharge generated with multiple pulse cycles, the overlap and intersection of the molten pool further led to the emergence of the low-angle boundary. The nickel-based, single-crystal superalloy is mainly composed of the γ phase and γ′ phase.

The formation of the recast layer is a result of rapid melt–solidification, a typical process with many special features. Figure 7 schematically shows the formation processes of the recast layer on the single-crystal superalloy. The pulse duration of EDM is very short. However, the highest temperature in the discharge process can increase rapidly over the melting point of the alloy. The γ phase and ordered $L1_2$ phase melt to form a liquid film. After the end of discharge, the cooling rate is more than 10^6 K/s, and the molten metal solidifies rapidly. The accelerated cooling rate prevents precipitation. In this process, the higher directional temperature gradient field makes the recast layer epitaxially grow along the matrix. At the same time, severe thermal stress generates, resulting in a much higher dislocation density in the recast layer region than that in the matrix region.

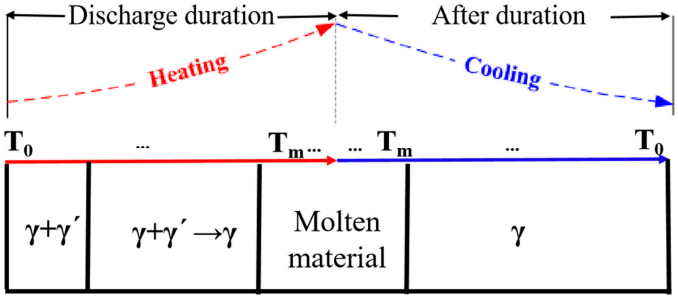


Figure 7. Schematic diagram of recast layer evolution of the fourth-generation single-crystal superalloy after EDM.

The recast layer around the cooling hole no longer contains the precipitated strengthening phase γ′, so the hardness may be lower than the matrix with precipitation.

Figure 8 shows the nanoindentation hardness of the film cooling hole wall at different locations along the hole wall–matrix direction (x direction) and the hole inlet–hole outlet direction (y direction). In Figure 8a, the position far away from the hole wall is larger than 7 GPa. The three testing points in Figure 8b are all located on the recast layer, and the hardness for all is smaller than 5 GPa. Compared with the hardness, point 1 in Figure 8a at 3 μm near the hole wall may be adjacent to the recast layer. The nanohardness of point 2 and point 3 in Figure 8a is not much different, and both are greater than point 1. Moreover, point 2 and point 3 are 11 μm and 19 μm away from the hole wall, respectively, and could be confirmed on the matrix due to the small range of the heat-affected zone [19]. Based on Figure 8a,b, it can be considered that the recast layer of the hole wall is much softer than the nearby alloy matrix. In addition, the nanohardness is lower than 5 GPa, while the hardness of the matrix in Figure 8a is greater than 7 GPa. The hardness of the recast layer is lower than that of the matrix, which agrees with the microstructure analysis above. The molten metal is remelted and solidified to adhere to the hole wall, and the recast layer is determined to be a single-phase γ structure using various analysis methods and does not contain precipitated strengthening γ′ phase, so the overall hardness value is low.

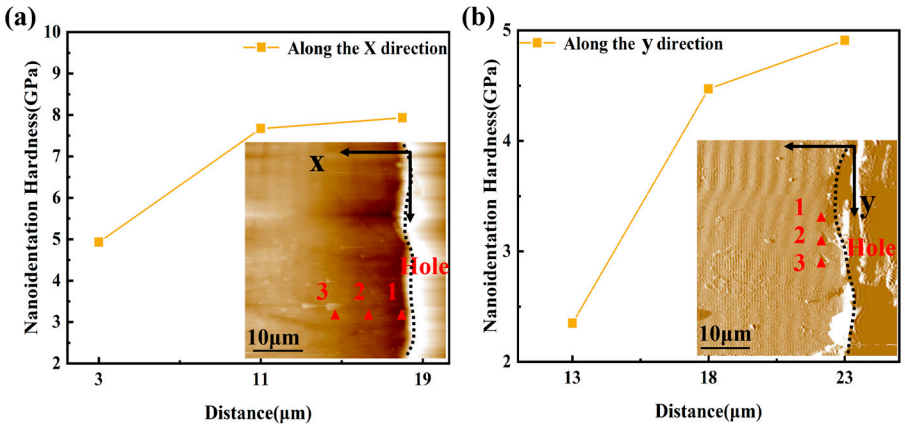


Figure 8. Nanoindentation hardness of the recast layer and matrix at different positions. (**a**) Schematic diagram of nanoindentation hardness and indentation of the recast layer and matrix in the x direction. (**b**) Schematic diagram of nanoindentation hardness and indentation of the recast layer in the y direction. The hardness of the recast layer is much lower than that of the matrix, caused by the lack of precipitation.

Considering the varied nanohardness of the recast layer at different positions, the different mechanical behavior between the recast layer and the matrix may be a weakness at the crack initiation point. In the future, it is necessary to further confirm the hardness evolution of the recast layer during service. Moreover, the different oxidation behavior may be exhibited for different thicknesses of the recast layer.

5. Conclusions

In this work, the microstructure and crystal structure of the recast layer of a single-crystal superalloy after EDM were studied using FIB and HR-TEM. The recast layer is formed by a localized molten pool induced with drilling, which undergoes directional solidification with a specific temperature gradient, and epitaxial growth occurs along the single-crystal alloy matrix. The recast layer has a single-phase structure composed of a supersaturated γ phase with the same orientation in the matrix. In the recast layer, there are plenty of defects, and its lattice constant is larger than that in the matrix due to the supersaturated solutions. It is determined that the recast layer has the characteristics of a rapid solidification nonequilibrium structure. There is a small mismatch between the recast layer and the matrix. The nano-indentation test confirms that the hardness of the recast layer near the hole wall is lower than that of the nickel-based, single-crystal superalloy substrate, which might affect the creep performance of the blade. The recast layer distributed on the film cooling hole wall easily falls off the surface of the alloy due to the difference in the formation mode and the structure of the matrix.

Author Contributions: Conceptualization, Z.Y.; data Curation, L.L. and J.W.; formal analysis, Z.Y. and L.L.; resources, Z.Y.; writing—original draft preparation, Z.Y. and L.L.; supervision, J.W. and J.X.; validation, W.Z. and L.Z.; writing—review and editing, F.H. and Z.W.; project administration, Z.W. All authors have read and agreed to the published version of the manuscript.

Funding: The authors are grateful for support from the Research Fund of the State Key Laboratory of Solidification Processing (NPU), China (Grant No. 2022-BJ-03).

Data Availability Statement: The data presented in this study are available on request from the corresponding author.

Conflicts of Interest: The authors declare that they have no conflict of interest.

References

1. Miller, R.A. Thermal barrier coatings for aircraft engines: History and directions. *J. Therm. Spray Technol.* **1997**, *6*, 35–42. [CrossRef]
2. He, K. Investigations of film cooling and heat transfer on a turbine blade squealer tip. *Appl. Therm. Eng.* **2017**, *110*, 630–647.
3. Liu, Y.; Ru, Y.; Zhang, H.; Pei, Y.; Li, S.; Gong, S. Coating-assisted deterioration mechanism of creep resistance at a nickel-based single-crystal superalloy. *Surf. Coat. Technol.* **2021**, *406*, 126668. [CrossRef]
4. Wieghardt, K. *Hot-Air Discharge for De-Icing*; Wright Field, Air Materiel Command: Dayton, OH, USA, 1946; pp. 1–44.
5. Bunker, R.S. A Review of Shaped Hole Turbine Film-Cooling Technology. *J. Heat Transf. Trans. Asme* **2005**, *127*, 441–453. [CrossRef]
6. Ay, M.; Çaydaş, U.; Hasçalık, A. Optimization of micro-EDM drilling of inconel 718 superalloy. *Int. J. Adv. Manuf. Technol.* **2013**, *66*, 1015–1023. [CrossRef]
7. Tao, X.; Liu, Z.; Qiu, M.; Tian, Z.; Shen, L. Research on an EDM-based unitized drilling process of TC4 alloy. *Int. J. Adv. Manuf. Technol.* **2018**, *97*, 867–875. [CrossRef]
8. Li, C.; Xu, X.; Li, Y.; Tong, H.; Ding, S.; Kong, Q.; Zhao, L.; Ding, J. Effects of dielectric fluids on surface integrity for the recast layer in high speed EDM drilling of nickel alloy. *J. Alloys Compd.* **2019**, *783*, 95–102. [CrossRef]
9. Pei, H.Q.; Wang, J.J.; Li, Z.; Li, Z.W.; Yao, X.Y.; Wen, Z.X.; Yue, Z.F. Oxidation behavior of recast layer of air-film hole machined by EDM technology of Ni-based single crystal blade and its effect on creep strength. *Surf. Coat. Technol.* **2021**, *419*, 127285. [CrossRef]
10. Kuppan, P.; Rajadurai, A.; Narayanan, S. Influence of EDM process parameters in deep hole drilling of Inconel 718. *Int. J. Adv. Manuf. Technol.* **2008**, *38*, 74–84. [CrossRef]
11. Wang, F.; Liu, Y.; Shen, Y.; Ji, R.; Tang, Z.; Zhang, Y. Machining Performance of Inconel 718 Using High Current Density Electrical Discharge Milling. *Mater. Manuf. Process.* **2013**, *28*, 1147–1152. [CrossRef]
12. Tang, J.; Yang, X.A. novel thermo-hydraulic coupling model to investigate the crater formation in electrical discharge machining. *J. Phys. D Appl. Phys.* **2017**, *50*, 365301. [CrossRef]
13. Tang, J.; Yang, X. Simulation investigation of thermal phase transformation and residual stress in single pulse EDM of Ti-6Al-4V. *J. Phys. D Appl. Phys. A Europhys. J.* **2018**, *51*, 135308. [CrossRef]
14. Cusanelli, G.; Hessler-Wyser, A.; Bobard, F.; Demellayer, R.; Perez, R.; Flükiger, R. Microstructure at submicron scale of the white layer produced by EDM technique. *J. Mater. Process. Technol.* **2004**, *149*, 289–295. [CrossRef]
15. Murray, J.W.; Fay, M.W.; Kunieda, M.; Clare, A.T. TEM study on the electrical discharge machined surface of single-crystal silicon. *J. Mater. Process. Technol.* **2013**, *213*, 801–809. [CrossRef]
16. Liu, J.F.; Guo, Y.B.; Butler, T.M.; Weaver, M.L. Crystallography, compositions, and properties of white layer by wire electrical discharge machining of nitinol shape memory alloy. *Mater. Des.* **2016**, *109*, 1–9. [CrossRef]
17. Li, C.; Zhang, B.; Li, Y.; Tong, H.; Ding, S.; Wang, Z.; Zhao, L. EDM/ECM high speed drilling of film cooling holes. *J. Mater. Process. Technol.* **2018**, *262*, 95–103. [CrossRef]
18. Dong, T.; Gao, C.; Li, L.; Pei, Y.; Li, S.; Gong, S. Effect of substrate orientations on microstructure evolution and stability for single crystal superalloys in rapid solidification process. *Mater. Des.* **2017**, *128*, 218–230. [CrossRef]
19. Shang, Y.; Zhang, H.; Hou, H.; Ru, Y.; Pei, Y.; Li, S.; Xu, H. High temperature tensile behavior of a thin-walled Ni based single-crystal superalloy with cooling hole: In situ experiment and finite element calculation. *J. Alloys Compd.* **2019**, *782*, 619–631. [CrossRef]
20. Shi, Z.X.; Liu, S.Z.; Yue, X.D.; Wang, Z.C. Effect of Long Term Aging at 980 °C on Microstructure Stability of DD15 Single Crystal Superalloy. *Fail. Anal. Prev.* **2020**, *15*, 217–220.

Disclaimer/Publisher's Note: The statements, opinions and data contained in all publications are solely those of the individual author(s) and contributor(s) and not of MDPI and/or the editor(s). MDPI and/or the editor(s) disclaim responsibility for any injury to people or property resulting from any ideas, methods, instructions or products referred to in the content.